Insights on the state of stress in the mantle beneath Pahala, Hawai'i

John D. Wilding *[α] and Zachary E. Ross[α]

[α] Seismological Laboratory, California Institute of Technology, Pasadena, CA, USA.

Abstract

Magma supply rates from the mantle to Hawaiian volcanoes serve as an important control on eruptive behavior at the surface. The Pāhala Sill Complex, a collection of magma-bearing, seismogenic structures at 40 km depth beneath Hawai'i, presents an opportunity to elucidate interactions between stress and magma transport processes in the mantle. We invert for full moment tensors of sill earthquakes and identify predominantly shear mechanisms with persistent tensile faulting components. Slip occurs in-plane with the sill structures. Pressure axes are radially oriented about a point near Mauna Loa, consistent with a stress field generated by a flexural load. Together, these observations suggest that magma flux through the sill structures generates seismicity by increasing pore pressure and promoting slip. Our results suggest that stress changes in mantle structures may enable fluctuations in magma supply rates to the surface over short timescales.

Keywords: Moment tensor inversion; Kilauea; Mauna loa; Magma transport; Deep volcano plumbing.

1 Introduction

The rate at which magma is supplied to a volcano's near-surface storage reservoirs from its deep plumbing system exerts a primary control on the character and rate of eruptive activity. Early work on supply rates to Kīlauea posited that historic magma supply rates were effectively constant [Swanson 1972]. More recent studies have shown that significant variations in magma supply may occur on timescales ranging from years to centuries [Dvorak and Dzurisin 1993; Swanson et al. 2014; Anderson and Poland 2016]. These fluctuations may affect eruptive productivity at Kīlauea and additionally modulate the transition from effusive to explosive eruptions [Swanson et al. 2014]. A growing body of work suggests that activity in deep magma plumbing systems can influence eruptive behavior at the surface over relatively short timescales (e.g., days to months) [Shapiro et al. 2017; Cesca et al. 2020; Greenfield et al. 2022]. Understanding the deep structures and processes responsible for magma transport to the surface is thus crucial to analyzing the dynamics of shallow activity and may be important for improving the resolution of eruption forecasting [Dzurisin and Poland 2019].

Elastic modeling and analog experiments indicate that the state of stress in the mantle can play an important role in the development of ocean island volcano magma structures at multiple scales, which in turn affect inter-volcano spacings [Hieronymus and Bercovici 1999] and the localization of individual magma bodies and cracks [Rubin 1995; Watanabe et al. 2002; McGovern 2007]. Interactions between the stress state of the mantle and the evolution of magma transport pathways are evinced by the subhorizontal mantle fault zone beneath south Hawai'i [Wolfe et al. 2003], which likely formed due to flexural stresses [Pritchard et al. 2007] but is thought to represent a pathway for lateral magma transport from the hotspot to Kīlauea [Wright and Klein 2006; Wech and Thelen 2015]. Although stress is recognized as a primary control on the long-term development of the deep plumbing system, its influence on short-term magma transport dynamics is less well established.

* jwilding@caltech.edu

Transient, mantle-driven surges in magma supply to Hawaiian volcanoes have been observed, but the factors that enable this behavior remain poorly understood [Dzurisin and Poland 2019]. One such surge to Kīlauea and Mauna Loa was documented between 2003-2007 [Poland et al. 2012]; more recently, an ongoing 2015- surge has been suggested [Burgess and Roman 2021]. The present surge has been accompanied by a mantle earthquake swarm below 30 km depth beneath the town of Pāhala, characterized by seismicity rates which are several orders of magnitude larger than the typical background rate for the region [Burgess and Roman 2021]. Wilding et al. [2023] performed waveform relocation of these earthquakes and identified a 10 x 16 x 7 km collection of subhorizontal sheeted structures which they termed the Pāhala Sill Complex (PSC) (Figure 1). On the basis of the PSC's proximity to a tremor-generating volume [Aki and Koyanagi 1981; Wech and Thelen 2015], diffusively migrating seismicity through the structures, long-period earthquakes, and previous work suggesting that Hawai'i's deep plumbing system may intersect with the PSC region [Wright and Klein 2006], Wilding et al. [2023] identified the PSC as a major magma transport feature. Studying the PSC might provide an opportunity to elucidate magma processes in the Hawaiian mantle. The intense seismic activity of the PSC also raises further, related questions regarding magma dynamics within the sills: namely, why apparent magma transport is so seismogenic in PSC structures, and how these structures might regulate magma flux.

In order to investigate the influence of stress on magma transport processes within the PSC, we perform moment tensor inversion for 9,472 events from the Wilding et al. [2023] catalog. We use P-wave amplitude data and implement an automated P-wave amplitude measurement procedure. Our workflow also involves calculating the event spectra of target events to ensure that amplitudes are measured in an appropriate frequency band for each event. Moment tensor inversions are performed as Bayesian inference problems, allowing us to fully characterize uncertainties in moment tensor components, and include empirical corrections for 3D attenuation structure. Most solutions are shear-dominated with a positive isotropic

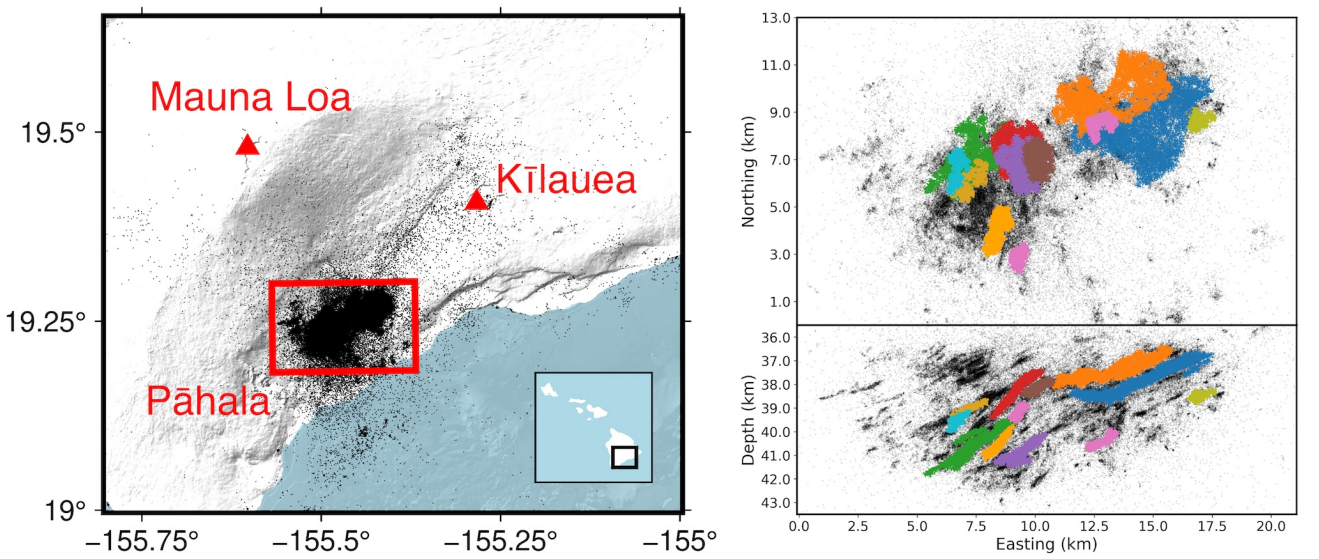

Figure 1: Overview of south Hawai'i. Left: Location of the Kīlauea and Mauna Loa summits and the Pāhala Sill Complex (PSC) swarm (boxed). Seismicity below 30 km depth from the Wilding et al. [2023] catalog is plotted. Right: map view and cross-section of seismicity in the boxed region. Individual structures are colored for clarity.

source component consistent with a faulting process precipitated by high pore pressure. Observed faulting geometries are consistent with a flexural stress field produced by the Hawaiian island load and suggest that flexure provides the necessary conditions for seismogenic magma transport in the mantle.

2 Methods

Our data consist of vertical-component velocity waveforms recorded on the HV (Hawaiian Volcano Observatory Network) and PT (Pacific Tsunami Warning Seismic System) seismic networks on the island of Hawai'i [USGS Hawaiian Volcano Observatory (HVO) 1956; Pacific Tsunami Warning Center 1965]. We select waveforms for analysis using the P wave arrival times of the Wilding et al. [2023] catalog, which were produced by the automated picking algorithm PhaseNet [Zhu and Beroza 2019]. The catalog spans November 2018 to April 2022.

Body wave amplitude measurements are one of the various data types commonly used in moment tensor inversions [Fitch et al. 1980; Ebel and Bonjer 1990; Kwiatek et al. 2016]. Here, we restrict ourselves to the use of signed P-wave amplitude data, which can more easily be measured by an automated process than signed S-wave amplitudes. The amplitudes of the first swings of P waves are an accurate representation of the radiation pattern in the point source approximation, so the P-wave amplitude must be measured over sufficiently low frequencies to exclude finite-faulting effects. Although the Wilding et al. [2023] catalog does not report magnitudes, the Hawaiian Volcano Observatory (HVO) earthquake catalog reports a magnitude range M_L 0.98–4.67 in the PSC over the period spanned by the catalog [USGS Hawaiian Volcano Observatory (HVO) 1956]. Over this magnitude range, event spectra and corner frequencies may vary considerably, so reliable measurements cannot be attained within a uniform frequency band. A conservatively chosen frequency band that represents the largest events as a point source would result in diminished SNR for the smaller events; conversely, measurements at higher frequencies can improve the SNR of smaller arrivals but may introduce finite-faulting effects for measurements of the larger earthquakes.

2.1 Determining optimal frequency bands for each event

To ensure our amplitude measurements occur over an appropriate frequency range for each event, we perform spectral decomposition [Shearer et al. 2006] to estimate the source spectra and corner frequencies of each target event. Below, we summarize our methodology, which adheres closely to the steps outlined in Trugman and Shearer [2017].

We identify 66,048 events within the PSC with at least 20 P-wave picks. For each pick, we define a noise window (2.3 to 0.3 seconds before the P-wave arrival) and a signal window (0.3 seconds before to 1.7 seconds after the P-wave arrival). Our 2 second window is shorter than that employed by Trugman and Shearer [2017]; we selected this length after manual inspection of several waveforms revealed high-amplitude secondary phases arriving approximately 2 s after the P-wave onset. Spectra are computed from vertical-component velocity waveforms using the mtspec software package [Prieto et al. 2009; Prieto 2022] with a time-bandwidth product of 3.5 and 5 tapers, then converted to displacement. We filter for high-quality spectra by requiring that the mean spectral amplitude of the signal window exceed the mean spectral amplitude of the noise window over five non-overlapping frequency bands from 2.5-25 Hz. We discard events with less than 5 recordings meeting these criteria, resulting in 15,075 target events.

We use these spectra to solve an overdetermined linear system of equations for event terms at each frequency point

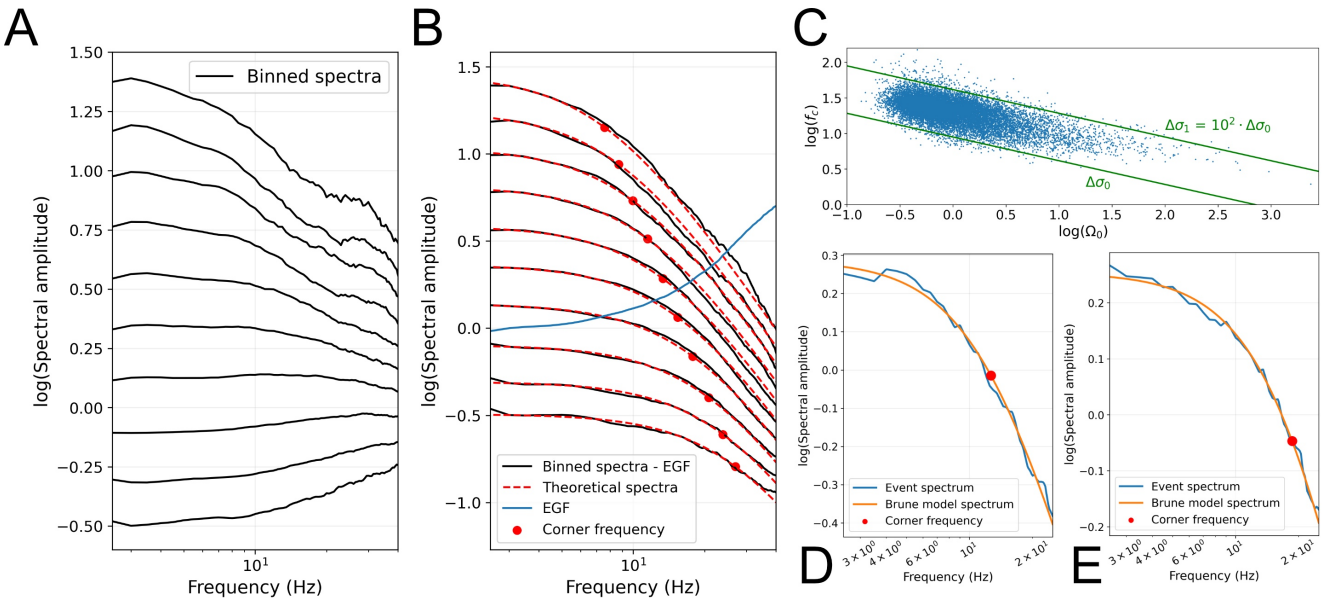

Figure 2: Results of the spectral decomposition procedure. (a) Event spectra binned by spectral moment. (b) EGF-corrected binned spectra and theoretical spectra for a Brune model. The EGF is determined by the best-fitting $[\epsilon_0, \epsilon_1]$ parameter vector. (c) Corner frequencies f_c and low-frequency spectral asymptotes Ω_0 for our target events. Green lines are plotted for two theoretical $\Delta\sigma$ values, with $\Delta\sigma_1$ greater than $\Delta\sigma_0$ by 2 orders of magnitude. The majority of retrieved $\Delta\sigma$ values are within this range. (d-e) Examples of spectral fitting to determine corner frequency.

$$\log_{10}(d_{ij}) = \log_{10}(e_i) + \log_{10}(tt_{ij}) + \log_{10}(st_j) \quad (1)$$

where d_{ij} is the recorded spectral amplitude of event i at station j, e_i is the event term of event i, tt_{ij} is a travel-time term (discretized in 1-second bins), and st_j is the station term of station j. Because we do not remove instrument response, the station term is informed by contributions from near-site effects and the transfer function of the recording instrument. HVO reported changes to the instrument responses of stations AIND, ALEP, KIND, NAHU, OTLD, and UWE during the study period [USGS Hawaiian Volcano Observatory (HVO) 1956], so for these stations we define separate station terms before and after the instrument response change. We solve the system of linear equations at each frequency point between 2.5 and 25 Hz using an iteratively reweighted least-squares technique to suppress the influence of outliers.

The retrieved event terms represent relative spectra in the logarithmic domain. To determine corner frequencies of individual events, an empirical Green's function (EGF) must be subtracted from all spectra to retrieve absolute spectra. We employ a stacking approach following Trugman and Shearer [2017]. We bin event spectra by mean log amplitude over the 2.5-4 Hz frequency band (Figure 2a), using a bin width of 0.2 logarithmic units. We exclude high- and low-amplitude bins that contain insufficient events and are contaminated by high-frequency noise. We then calculate theoretical spectra for each bin by parameterizing the logarithm of stress drop as

$$\log_{10}(\Delta\sigma) = \epsilon_0 + \epsilon_1 \Omega_0 \quad (2)$$

where $[\epsilon_0, \epsilon_1]$ is a parameter vector defining the stress drop-moment scaling relationship and Ω_0 is the low-frequency asymptote of the spectrum. This approach allows some deviation from self-similar earthquake scaling, as expressed by the ϵ_1 parameter. The binned spectra are subtracted from the theoretical spectra, and the residuals from each bin are stacked to form an EGF. We calculate a misfit by evaluating the L2 norm between the theoretical spectra and the EGF-corrected binned spectra. We grid search over values of ϵ_0 and ϵ_1 to minimize this misfit, first resampling the spectra in the log domain to suppress the influence of noise at higher frequencies.

The best-fitting combination of values is $[\epsilon_0, \epsilon_1] = [2.9, 0.15]$, representing a slight deviation from self-similarity, consistent with previous applications of this technique [Trugman and Shearer 2017; 2018; Trugman 2020] (Figure 2b). For each event, we subtract the retrieved EGF to convert the relative event spectrum into an absolute spectrum, resample the spectrum at evenly spaced points in the logarithmic domain, and fit a Brune source model [Brune 1970],

$$\Omega(f) = \frac{\Omega_0}{1 + (\frac{f}{f_c})^2} \quad (3)$$

where Ω is spectral amplitude, f is frequency, and f_c is the corner frequency (see Figure 2d-e for examples). Retrieved Ω_0 and f_c values imply a range of stress drops spanning approximately two orders of magnitude, consistent with observations of other earthquake sequences (Figure 2c) [Trugman and Shearer 2017; Shearer et al. 2022]. For 30 events, event spectra are too flat over the 2.5 to 25 Hz frequency band for reliable f_c values to be determined (these are excluded from the figure).

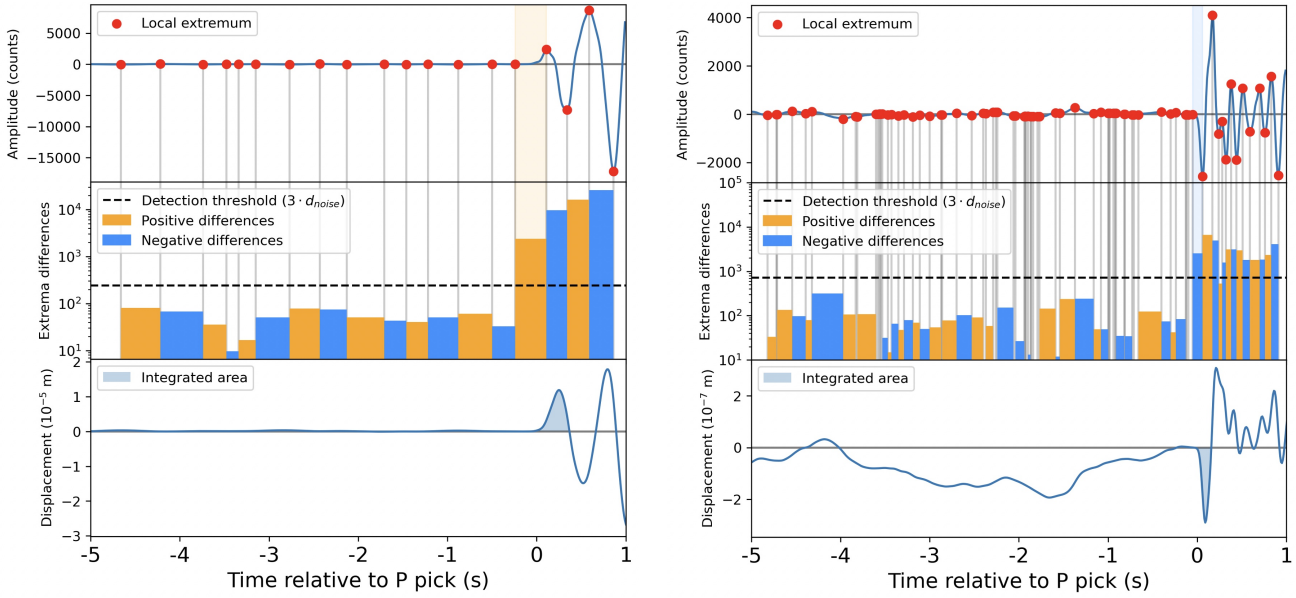

Figure 3: Illustration of the automated amplitude measurement procedure for a high-SNR (left) and a low-SNR (right) waveform. Top panel: raw instrumental velocity waveform, with local extrema plotted. Middle panel: differences between each pair of consecutive local extrema. The first swing of the P-wave occurs between the first pair of extrema whose absolute difference surpasses the detection threshold $3 \cdot d_{noise}$. Bottom panel: Displacement waveform with instrument response removed. The shaded region is integrated to measure the P-wave amplitude. All steps in this procedure are automated.

2.2 Automated P-wave amplitude measurements

With corner frequency estimates available for 15,075 events, we can measure P-wave amplitudes in a frequency band appropriate for each event. We measure P-wave amplitudes by integrating the first swing of the phase arrival on a vertical-component displacement waveform [Kwiatek et al. 2016]. For each event, we take measurements in a passband of 1 Hz to f_c Hz, which we take to adequately approximate the frequency range over which the spectrum is flat. If $f_c > 20$ Hz, we filter from 1 to 20 Hz. To measure amplitudes systematically across all events, we employ an automated technique which examines the waveform for sudden changes in the differences between consecutive local extrema. Our methodology for a single waveform recording is described next.

We define a to 4.75 s-long noise window starting 5 s before the picked P-wave arrival and a 1.75 s-long signal window starting 0.25 before the pick. We require the variance of the signal window to exceed the variance of the noise window by a factor of 30; otherwise, the waveform is discarded. Next, we determine the polarity of the first swing and estimate the approximate onset time using the raw velocity waveform recorded by the instrument. To do so, we identify all local extrema (peaks and troughs) in the combined noise and signal windows. We then calculate the differences between all consecutive pairs of local extrema; these values include peak-to-trough and trough-to-peak values, but for simplicity of terminology we refer to them as extrema differences. We define d_{noise} as the maximum absolute extremum difference in the noise window. The first swing of the P-wave arrival is tentatively identified by finding the first pair of extrema in the signal window with a difference $> |3 \cdot d_{noise}|$. This extrema difference must meet two further conditions designed to filter out waveforms with emergent arrivals: the preceding absolute extrema difference must be smaller by a factor of at least 5, and no earlier absolute peak-to-trough difference can exceed $|1.2 \cdot d_{noise}|$. If these conditions are not met, the waveform is discarded. If these conditions are met, the approximate swing onset time t_{start} is determined as the time of the first extremum in the selected extrema pair, and the polarity is determined as up if the selected extrema difference is positive or down if the difference is negative. See Figure 3 for a visual explanation of these steps.

If an approximate onset time and polarity are successfully determined, the instrument response is deconvolved, the waveform is converted to displacement, and the amplitude of the displacement waveform at t_{start} is subtracted from the signal. Next, we identify the time range which spans the first swing. The beginning of the first swing is identified as the first zero crossing after t_{start} with the correct polarity (negative-to-positive for up; positive-to-negative for down). The end of the first swing is identified as the next zero crossing of the waveform. Two further checks are implemented to ensure that the measurement is not contaminated by low- or high-frequency noise: the number of local extrema within the swing must not exceed 3, and the swing end must be at least 0.05 seconds (5 samples) later than the swing start. If these conditions are not met, the waveform is discarded; otherwise, we integrate the waveform between the swing start and swing end and record the measurement.

The quality control checks that we implement cause many waveforms with insufficient SNR to be discarded. However,

we can take advantage of the spatial density of earthquakes within the PSC to identify highly similar P-wave arrivals from nearby events that may have higher SNR. We can then measure a P-wave amplitude for a low-SNR event by rescaling and measuring the amplitude of a higher-SNR waveform. The steps involved in this procedure are described below.

If the measurement procedure fails for a given waveform, we identify all events within 0.5 km of the target event that have picks on the same station. For each neighboring event, we retrieve its recorded P waveform, filter from 1 to f_c Hz, and cross-correlate the neighboring event signal with the target event signal. Cross-correlation is performed using a 1.5 s window from 0.5 s before to 1.0 s after the neighboring event's P-wave pick. If the maximum cross-correlation coefficient is greater than 0.9, we scale the amplitude of the neighboring event waveform to the amplitude of the original event and re-attempt the measurement procedure described above on the rescaled waveform (see Figure 4 for examples of matched waveforms). We attempt this process on all neighboring events until a successful measurement is made, or all waveforms are discarded. This approach increases the number of events with ≥ 20 measured amplitudes from 3,900 to 9,472. For stations whose instrument response changed over the catalog period, we do not correlate event pairs which span the station response change.

We apply the measurement procedure to 652,291 picked P-wave arrivals from PSC events in the Wilding et al. [2023] catalog and record 361,792 total successful measurements. We empirically evaluate the accuracy of the measurements by randomly sampling 1000 waveforms and manually examining them for incorrectly picked first swings. Of these, we find that 6 have incorrectly picked first swings.

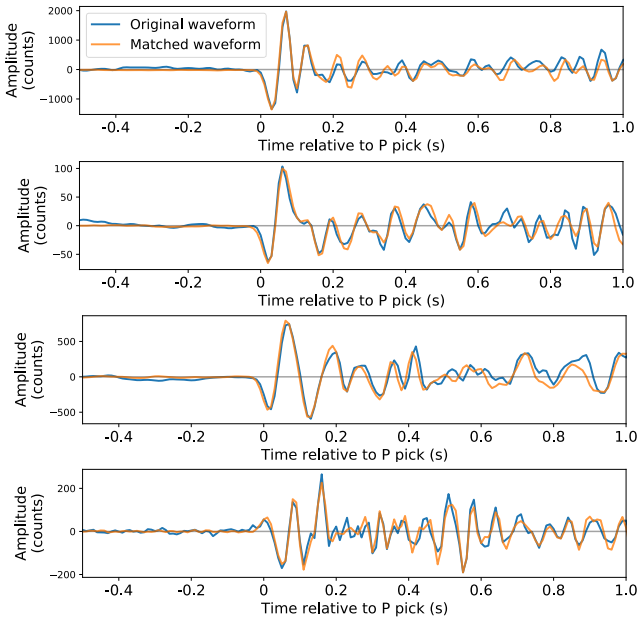

Figure 4: Examples of the waveform amplitude rescaling process. Several high-SNR waveforms are rescaled to the amplitude of low-SNR waveforms from neighboring events. In each case, the automated measurement procedure has failed on the low-SNR waveform; the high-SNR waveforms are rescaled to the amplitude of the low-SNR waveform and used to retrieve an amplitude measurement.

2.3 Moment tensor inversion procedure

Having obtained P-wave amplitude measurements within an appropriate frequency band for each event, we proceed to the moment tensor inversion. Following Fitch et al. [1980], we define our forward model as

$$u = \frac{\mathrm{P}(\mathbf{M}, \theta, \phi)\cos(\iota)}{4\pi\rho\alpha^3 r} \tag{4}$$

where u is the P-wave amplitude as measured on the vertical component, θ is the takeoff angle of the ray (measured from vertical downwards), ϕ is the source-receiver azimuth, ι is the incidence angle of the ray upon the station (measured from vertical downwards), r is the source-receiver distance, α is the P-wave velocity of the source region, ρ is the density of the host rock at the source, and P is the P-wave radiation pattern [Fitch et al. 1980]:

$$\begin{aligned}\mathrm{P}(\mathbf{M}, \theta, \phi) = &M_{xx}\sin^2\theta\cos^2\phi + M_{yy}\sin^2\theta\sin^2\phi + \\ &M_{zz}\cos^2\theta + M_{xy}\sin^2\theta\sin 2\phi + \\ &M_{xz}\sin 2\theta\cos\phi + M_{yz}\sin 2\theta\sin\phi.\end{aligned} \tag{5}$$

ι, θ, and ϕ are calculated using the relocated hypocenters of Wilding et al. [2023] and the linear gradient velocity model of Klein [1981]. Because the velocity model contains no layers deeper than 16.5 km, we use constant values of $\alpha = 8.3\,\mathrm{km\,s^{-1}}$ and $\rho = 3200\,\mathrm{kg\,m^{-3}}$ for all events. We also assume a constant velocity of $1.9\,\mathrm{km\,s^{-1}}$ at elevations above sea level. We use this linear forward model to relate the six independent moment tensor components $\mathbf{M} = [M_{xx}, M_{yy}, M_{zz}, M_{xy}, M_{xz}, M_{yz}]$ to P-wave amplitudes.

We formulate the moment tensor inversion problem as one of Bayesian inference to allow for each event's uncertainty to be quantified. For every event, we solve for a posterior distribution over the six moment tensor parameters using Stein variational gradient descent (SVGD) [Liu and Wang 2016], a variational inference procedure that has previously been applied to hypocenter and waveform inversion problems [Zhang and Curtis 2020; Smith et al. 2022]. The SVGD inference procedure represents posterior distributions as a particle cloud in six-dimensional $\mathbf{M}$ space with particle density proportional to probability density. We begin with a uniform prior over $\mathbf{M}$ and represent the data likelihood with a Huber density [Huber 1964; Schumann 2009]:

$$L = \exp(-H(u_{\mathrm{obs}} - u_{\mathrm{pred}})/\delta) \tag{6}$$

where u_{obs} is an observed amplitude, u_{pred} is the corresponding modeled amplitude, and H is the Huber loss:

$$H(x) = \begin{cases} \frac{1}{2}x^2 & \text{for } x > \delta \\ \delta(|x| - \frac{1}{2}\delta) & \text{otherwise.} \end{cases} \tag{7}$$

For measurements such that $|u_{\mathrm{obs}} - u_{\mathrm{pred}}| \leq \delta$, the Huber loss is proportional to an L2 norm and the Huber density is pro-

portional to a Gaussian distribution with $\sigma = \delta$. For measurements such that $|u_{\text{obs}} - u_{\text{pred}}| > \delta$, the Huber loss is proportional to an L1 norm and the Huber density is proportional to a Laplace distribution. Thus, the Huber density is fatter-tailed than the Gaussian distribution, providing additional robustness to outliers.

While the mean of the posterior distribution should be largely insensitive to δ, this parameter does control the scale of the distribution. Therefore, δ must be selected carefully to adequately reflect measurement uncertainty. Because our inversions are performed iteratively (see next section), we can select an appropriate value of δ by taking the (global) median absolute deviation (MAD) of amplitude residuals u_{res}. Amplitude measurements span several orders of magnitude, so for each u_{obs} we scale observed and predicted amplitudes to the focal sphere before calculating u_{res}:

$$u_{\text{obs}}^{\text{scaled}} = \frac{4\pi\rho\alpha^3 r}{M_0 \cos(\iota)} u_{\text{obs}} \tag{8}$$

$$u_{\text{pred}}^{\text{scaled}} = \frac{4\pi\rho\alpha^3 r}{M_0 \cos(\iota)} u_{\text{pred}} \tag{9}$$

$$u_{\text{res}} = u_{\text{obs}}^{\text{scaled}} - u_{\text{pred}}^{\text{scaled}} \tag{10}$$

where M_0 is the scalar moment of the event for which u_{obs} is recorded. $u_{\text{obs}}^{\text{scaled}}$ and $u_{\text{pred}}^{\text{scaled}}$ have been scaled to the focal sphere, so that $u_{\text{obs}}^{\text{scaled}} \in [-1, 1]$ and $u_{\text{pred}}^{\text{scaled}} \in [-1, 1]$. We calculate u_{res} for all measurements and define δ_0 as the MAD of all u_{res} values. The scalar value δ_0 is thus a scale-invariant estimate of the model misfit for all events. For each observation, we retrieve an appropriate δ value by rescaling δ_0 to the predicted amplitude:

$$\delta = \frac{M_0 \cos(\iota)}{4\pi\rho\alpha^3 r} \delta_0. \tag{11}$$

This procedure allows us to empirically derive uncertainties in a consistent way for our measurements across several orders of magnitude. At each iteration of the inversion, we calculate a new set of δ values using M_0 and u_{pred} values from the previous iteration. These values are not available for the first iteration, so for this step we manually set $\delta = u_{\text{obs}}$ for each observation.

We require a minimum of 20 observations to attempt an inversion. 9,472 events meet these criteria.

2.4 Empirical 3D structure corrections

While the posterior distributions characterize the moment tensor uncertainty originating from imperfect focal sphere coverage and errors in our automated measurements, they do not account for error arising from 3D heterogeneities in attenuation structure, which are widespread at Hawai'i [Lin et al. 2015] and may have a considerable effect on P wave amplitudes once integrated from the depth of the PSC (36-43 km) to the surface.

We perform additional corrections for unknown 3D structure by implementing a modified version of the hybridMT technique [Linzer 2005; Kwiatek et al. 2016]. Specifically, hybridMT iteratively corrects for unmodeled 3D structure and scattering effects on P-wave amplitudes similar to traditional station terms in hypocenter inversions. An initial set of moment tensor solutions is obtained and the ratio r = u_{pred} / u_{obs} is calculated for all observations, where u_{pred} are amplitudes predicted by the retrieved moment tensors and u_{obs} are observed amplitudes. Then, for each station j, the median $\tilde{r}_j$ of all u_{pred} / u_{obs} values recorded at the station defines an amplitude correction term, which is assumed to reflect contributions to recorded amplitudes from commonly sensed attenuation structure. $\tilde{r}_j$ is used to update that station's amplitude measurements:

$$u_j^{\text{updated}} = u_j^{\text{obs}} + w u_j^{\text{obs}} (\tilde{r}_j - 1), \tag{12}$$

where w is a weight term. The updated amplitude measurements are used to perform a new inversion, and the process is iterated until convergence of the station amplitude corrections. The hybridMT approach is effective at correcting for commonly sensed attenuation heterogeneities for events originating within a small source volume, so that raypaths can be assumed to roughly coincide. The PSC, however, has dimensions of approximately 10 x 16 x 7 km, so the common raypath assumption may not hold. For larger domains, Kwiatek et al. [2016] suggests defining distinct subdomains and running the iterative procedure separately within each domain, but this approach risks introducing edge effects near subdomain boundaries. Rather than arbitrarily partitioning the seismicity, we implement a source-specific version of hybridMT that utilizes local information. For each event i and station j, we define $\tilde{r}_{ij}$ as the median u_{pred} / u_{obs} ratio of events within a radius of Δ km around event i recorded on station j. $\tilde{r}_{ij}$ is then treated as a source-specific station amplitude correction and used to update the measured amplitude u_{ij}. This approach is similar to the source-specific station term approach introduced for travel-time corrections by Richards-Dinger and Shearer [2000]. We require a minimum of 30 nearby events for a source-specific station amplitude correction term to be calculated. Following Kwiatek et al. [2016], use a weight term w of 0.1. We tested several values of Δ between 1 and 10 km and found that the inversion results are largely insensitive to our choice of Δ. We select a value of $\Delta = 3.0$ km, the smallest integer value for which most events (8,730/9,472) have > 1000 neighbors. The source-specific approach introduced here results in smoothly varying amplitude correction terms across the PSC (Figure 5b). We evaluate the performance of the amplitude corrections by examining the decline in the MAD of u_{res} at each iteration; we find that the MAD is finished appreciably decreasing after 40 iterations and halt the iterative process at that step (Figure 5a).

The hybridMT technique can also aid in the detection of flipped polarities or unreliable station response information by examining the proportion of modeled polarities that match observed polarities at a given station. For 56 of the 61 stations used, polarity matching per station exceeds 90%; for 60 of the 61 stations, polarity matching exceeds 80%. At station HV-KUPD, however, polarity matching is 49%. This station is located near several stations in the lower east rift zone with

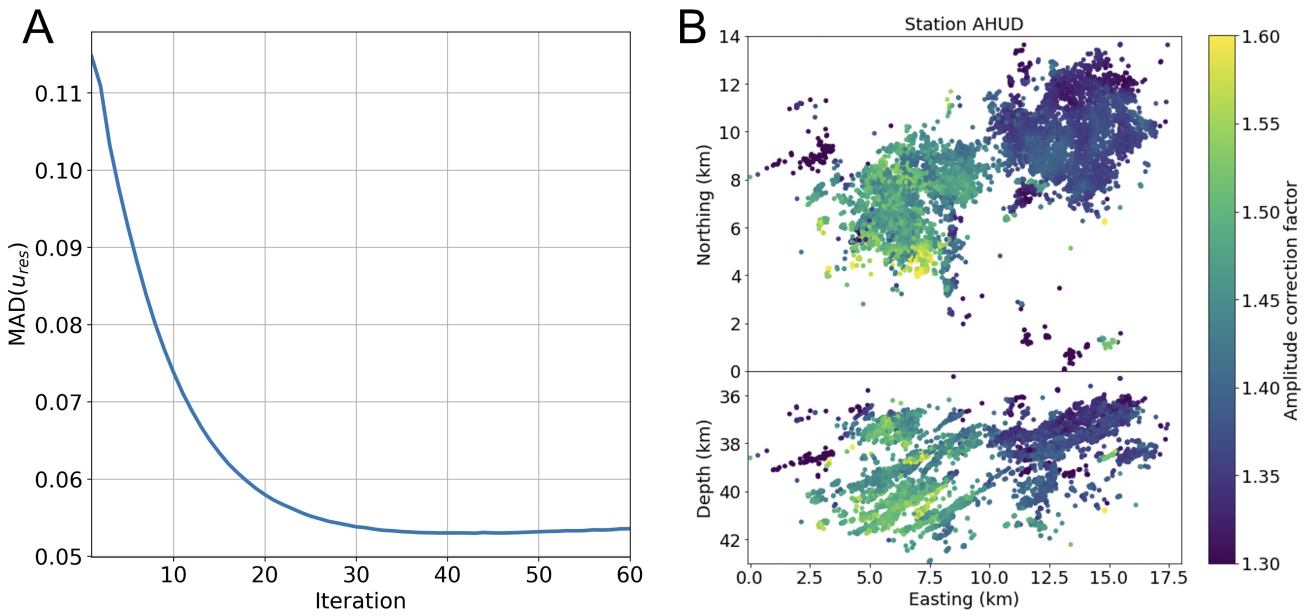

Figure 5: Illustration of the 3D structure amplitude correction procedure. (a) Decline in the median absolute deviation of amplitude residuals up to iteration 40. (b) Example amplitude correction factors for each event at station AHUD.

better polarity matching. Thus, we assume the misfit at station HV-KUPD is the result of unspecified instrumental effects and exclude its measurements from our inversion.

3 Results

3.1 Uncertainty analysis

In order to identify high-quality solutions from our set of inversion results, we examine confidence intervals (CIs) of several parameters: ISO%, CLVD%, and P and T axis dip and azimuth. ISO% and CLVD% represent the signed contributions of isotropic and compensated linear-vector dipole components to the moment tensor such that |ISO%| + |CLVD%| + DC% = 100, where DC% is the double-couple contribution. We employ the standard moment tensor decomposition described in Jost and Herrmann [1989] to compute ISO% and CLVD% values. To extract CIs for a given event, we calculate the value of these parameters for each point in the particle cloud representing the posterior probability distribution over $\mathbf{M}$. The 90% CI of a parameter is then defined as the range between the 5th and 95th percentiles of the values. The width of the 90% CI serves as an estimate of how well a parameter is constrained. P and T axis dip and azimuth angles are well-constrained for many events, with 39% (3696/9472) of events having CI width < 30° for all four angles. ISO% is also well-constrained, with 50% (4749/9472) of events having CI width < 14%. CLVD% is comparatively poorly constrained, with 50% (4759/9472) of events having CI width < 55%. The weaker constraints on CLVD% originate from a strong trade-off between CLVD and double-couple (DC) components in our solutions. For each solution, we estimate the magnitude of the trade-off between ISO%, CLVD%, and DC% by calculating the absolute Pearson correlation coefficient between the posterior ensemble of each pair of parameters. Histograms of correlation coefficients between ISO-CLVD, CLVD-DC, and ISO-DC are plotted in Figure 6. We observe moderate trade-offs in our solutions between ISO% and DC%, as well as between ISO% and CLVD%. DC% and CLVD% components, by contrast, have correlation coefficients > 0.9 for the vast majority of our solutions, indicating a nearly perfect trade-off. Significant trade-offs between DC and CLVD components have been noted as a feature of microseismic moment tensor inversions; Vavryčuk [2011] decomposed synthetic moment tensors and found that the retrieved CLVD% value was more sensitive to uniformly distributed noise than the ISO% value by a factor of approximately 3. Consequently, ISO% is generally better-constrained than CLVD% in our solutions.

To define a high-quality solution, we subset events for which ISO% CI width < 15%, CLVD% CI width < 55%, and P- and T- axis dip and azimuth CI width < 30° for all four angles. After applying these criteria, we retrieve 2,301 well-constrained events (example solution shown in Figure 7). The following analyses use these high-quality events only.

3.2 Validation against waveform-based moment tensor inversions

We validate a subset of our solutions by calculating complementary focal mechanisms using the cut-and-paste (CAP) waveform inversion method [Zhu and Helmberger 1996]. We select the five largest events for which we have solutions; these events range in magnitude from M_L 4.01 to M_L 4.55 [USGS Hawaiian Volcano Observatory (HVO) 1956]. For these events, clear surface wave arrivals are difficult to identify; because these events occur at depths ≥ 35 km, surface wave excitation is weak and susceptible to being overprinted by the body wave coda. Thus, we limit our inversion to *Pnl* waves. We filter *Pnl* waves between 0.2 and 0.5 Hz and perform bootstrap analysis to estimate uncertainties in the CAP solutions.

The results of the CAP inversion are compared against our solutions in Figure 8; waveform fit plots are provided in Figures S1-S5. Waveform fits are acceptable for all events. To facilitate comparison of our solutions and the CAP results, we plot only the double-couple contribution of our solutions. For all events except hv72856332, the best-fitting CAP result is very similar to our automated result. We note that our solution for hv72856332 is poorly constrained and is not classified as a high-quality solution according to the criteria laid out in section 3.1. The CAP bootstrap ensemble of solutions reflects a similarly high degree of uncertainty, and includes several solutions with differently oriented mechanisms that more closely resemble our automated solution. Because the inversion results for hv72856332 are poorly constrained across both inversion techniques, we infer that the available data are likely insufficient to calculate an adequate moment tensor solution. The fact that our solution for this event is flagged as low-quality suggests that our procedure to assess solution quality can successfully threshold low- and high-uncertainty solutions. On the basis of the close correspondence between the CAP results and our solutions for the other events tested here, we conclude that our inversion performs reasonably well for high-quality solutions.

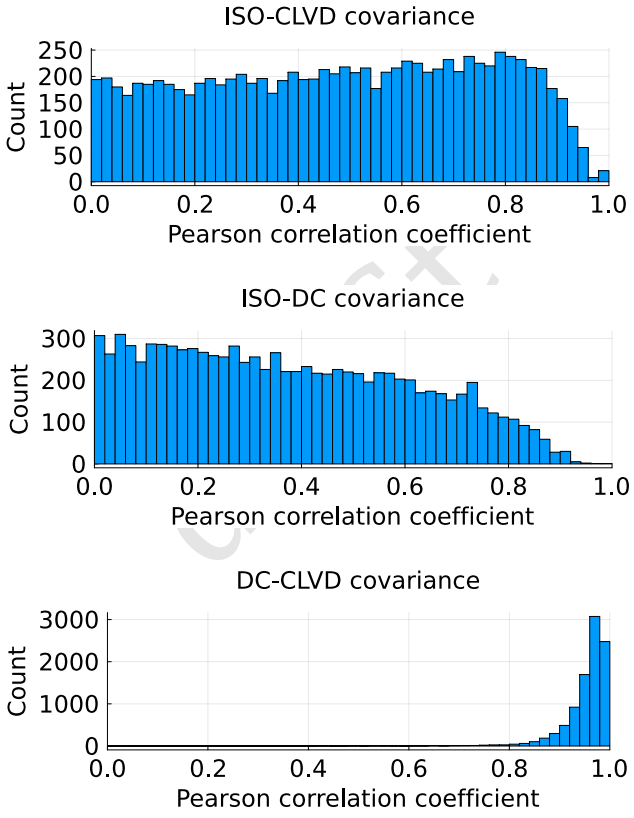

Figure 6: Histograms of the Pearson correlation coefficient between ISO, CLVD, and DC components for all solutions. DC and CLVD components have a much greater covariance than either ISO/DC or ISO/CLVD components, indicating significant trade-off.

3.3 Non-double-couple components

To determine the prevalence of non-double-couple components in our solutions, we plot the distribution of high-quality solutions on the moment tensor lune diagram (Figure 9) [Tape and Tape 2012]. The majority of moment tensors in this subset concentrate in a single mode on the lune corresponding to a slight positive isotropic component, with a mean ISO% of 11.7, indicating dominantly deviatoric mechanisms with a minor, but persistently observed, positive volume change. There exists greater variability in CLVD%, with a mean CLVD% of 1.6. This mode overlaps substantially with the crack line, although the mean CLVD% is too low to intersect the line; for an ISO% value of 11.7, an event on the crack line would have CLVD% = 9.4. We note that the crack line plotted here assumes a Poisson's ratio $\nu = 0.25$ [Tape and Tape 2012], and as such a tensile faulting mechanism may not align with the crack line if the local value of ν deviates from this standard value. Given the larger uncertainties in CLVD%, our results may still be consistent with tensile faulting along the $\nu = 0.25$ crack line. In order to test whether these moment tensors are compatible with a crack opening mechanism, we check whether the posterior distributions of each event encompass a solution on the crack line. We find that 73.1% of these events contain a crack opening mechanism within their posterior, suggesting that an interpretation of predominantly shear faulting with an additional tensile opening component is compatible with the majority of our solutions. We separately plot the full posteriors for mechanisms with 90% CI widths less than 5 and 25 for ISO% and CLVD%, respectively, and find that these mechanisms are clustered near the crack line (Figure 9). A smaller number of earthquakes contain a negative isotropic component (6.5% of well-constrained solutions), which may be attributable to complementary crack closing processes.

To examine whether this positive isotropic component is uniformly present throughout the PSC, we generate separate lune plots of high-quality solutions for 10 of the largest discrete structures in the sill complex (Figure 10). Discrete structures were identified by Wilding et al. [2023] using the DBSCAN clustering algorithm [Ester et al. 1996]. Of the 12 structures with the most events, two contain < 10 earthquakes with high-quality moment tensors and are excluded from plotting ("Sill 7" & "Sill 11"). Positive isotropic components are dominant within the largest two structures ("Sill 1" & "Sill 2"), which together host 45% of the high-quality solutions (1,031/2,301 events). While there is greater variability in the isotropic & CLVD components within smaller sills, earthquakes within all structures display predominantly positive isotropic components. The range of mean ISO% is between 7.2 and 17.1 for all sills shown here. These results indicate that a slight, yet significant, positive isotropic component is present for earthquakes distributed throughout the sill complex.

Although the relative locations of the Wilding et al. [2023] catalog are well-constrained, absolute location uncertainty for the catalog is on the order of 0-2 km. We undertake an additional analysis to examine the effect of absolute location error on the non-double-couple contributions to our moment tensor solutions. We expect our solutions to be robust with respect to kilometer-scale mislocation, because at the depth of the PSC

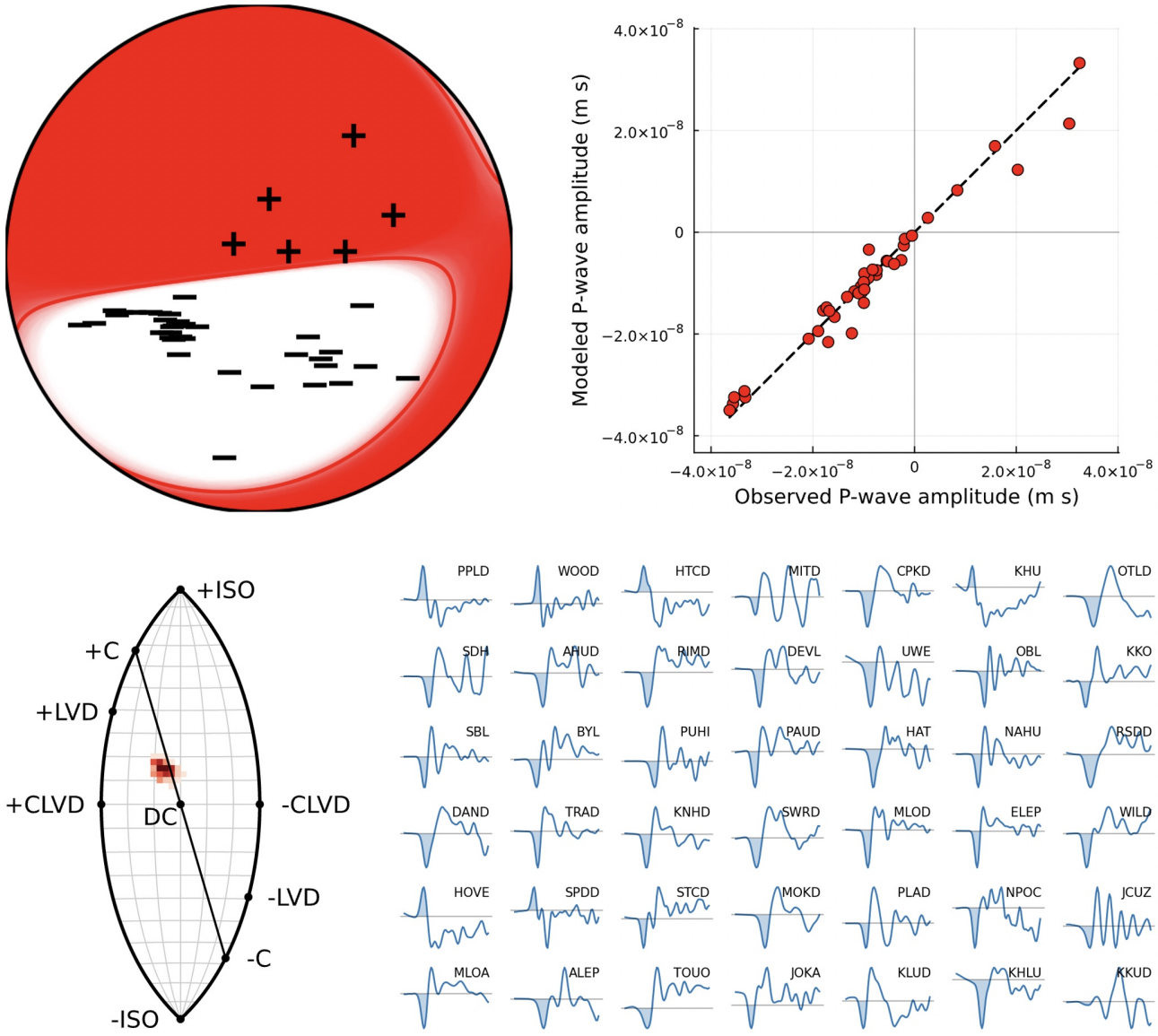

Figure 7: Example of the posterior distribution of a high-quality solution. Top left: ensemble of solutions in the posterior distribution; the mean solution is plotted with a solid red line. Plus and minus symbols indicate positive and negative first arrival polarities, respectively. Top right: observed and modeled P-wave amplitudes. Bottom left: ensemble of solutions plotted on the lune diagram. Bottom right: waveforms used in the inversion. Areas that are integrated to retrieve P-wave amplitudes are shaded in light blue. Each waveform spans 0.7 s and has been filtered from 1 to 14.8 Hz (the event's corner frequency).

(36-43 km), ray takeoff angles are relatively insensitive to shifts in hypocentral location. We run two tests. In the first, we shift hypocenter locations 5 km upward. In the second, we hold the hypocenters at their original depths and shift them 5 km to the northeast. The results of these tests are compared to the solution with original catalog locations in Figure S6. In both tests, the mean of the primary moment tensor mode shifts slightly but retains its positive isotropic component. We conclude that the positive isotropic component we observe is robust to reasonable absolute location errors.

Anisotropy in the earthquake source region, if unaccounted for, can introduce spurious non-double-couple components in moment tensor decompositions. The PSC, interpreted as a collection of sheeted magma-bearing structures, may host transverse isotropy with the symmetry plane aligned with the sill layering orientation, as has been observed in shallower melt structures [Jaxybulatov et al. 2014; Wu et al. 2023]. However, as we demonstrate in the next section, the slip plane for most of our solutions lies within the tangent plane of the sill, and by extension would also be aligned with the symmetry plane. Previous authors have demonstrated that spurious ISO and CLVD components are not introduced in transverse isotropy for pure shear slip within the symmetry plane [Vavryčuk 2018; Menke and Russell 2020]. We conclude that the isotropic components we observe are likely true reflections of positive volume change at the source.

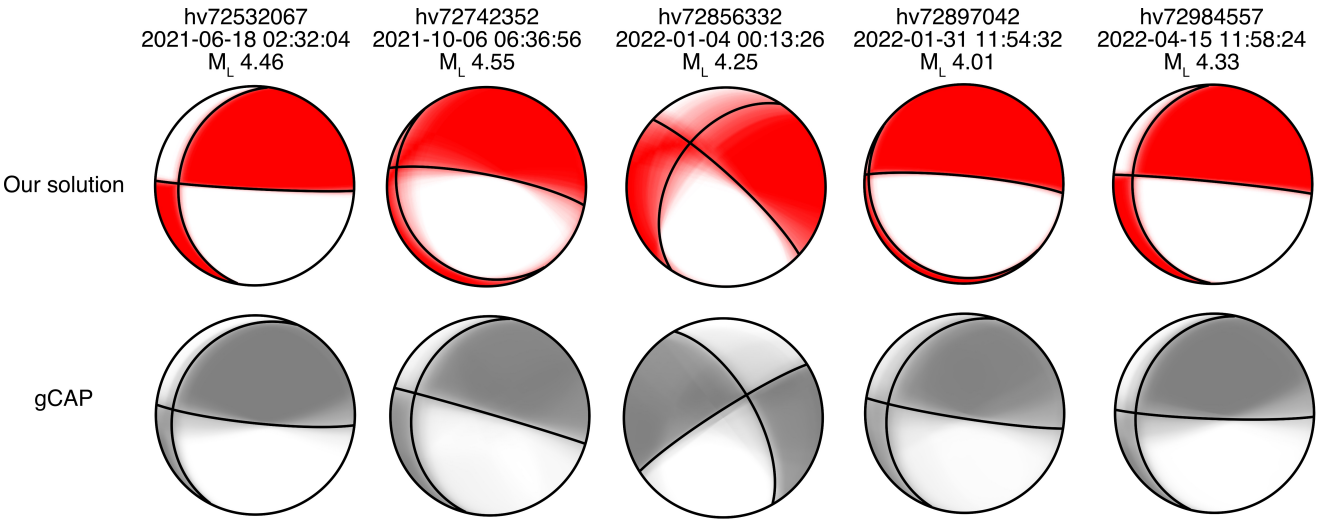

Figure 8: Comparison of inversion results for 5 $M_L \geq 4.0$ PSC events. Top row: solutions retrieved using our automated method. The best-fitting solution is plotted as a red line, and the ensemble of solutions from the solutions' posterior distribution are plotted in red. Bottom row: solutions retrieved using the CAP waveform inversion method. The best-fitting solution is plotted as a black line, and the ensemble of solutions from bootstrap analysis are plotted in gray. Only the double-couple components of our solutions are plotted to facilitate comparison with the CAP results.)

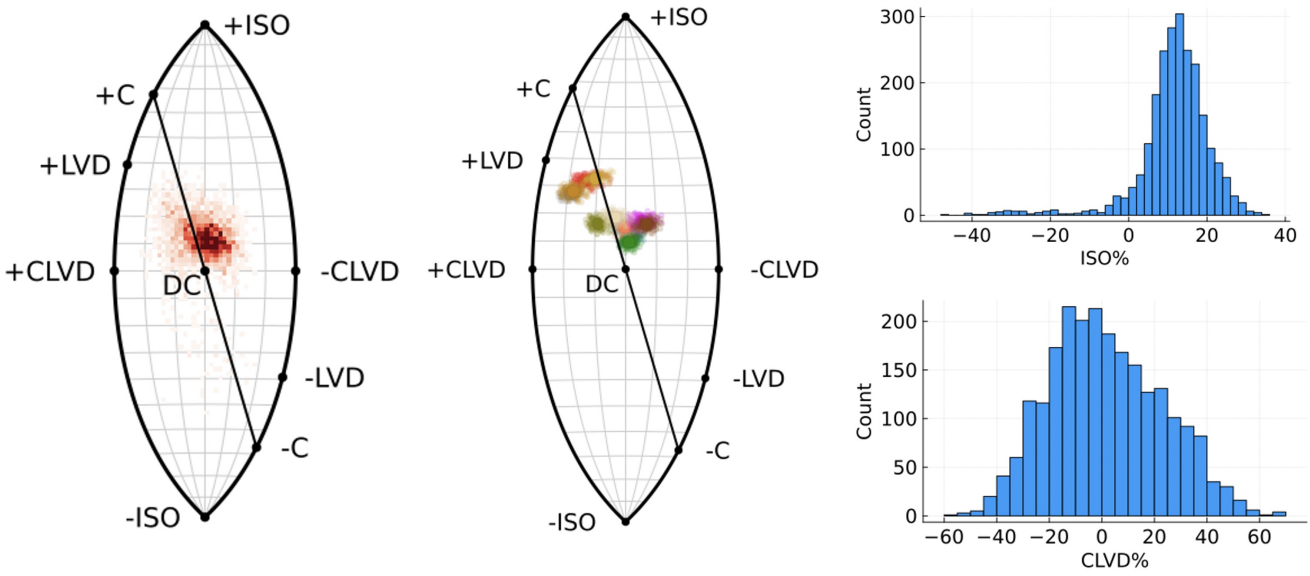

Figure 9: Illustration of non-double-couple components of high-quality solutions. Left panel: Heatmap on the lune diagram of all high-quality solutions. Middle panel: posteriors for the 12 best-constrained events. Right column: histograms of ISO% and CLVD% for the entire catalog, displaying a prominent positive isotropic mode among the high-quality solutions.

3.4 Faulting geometry

We observe that the majority of mechanisms have a nodal plane aligned with the local orientation of their host structure. We again spatially subset high-quality events by discrete structures and plot the DC components of radiation patterns of well-constrained events in Figure 11. For most earthquakes, we observe an excellent correspondence between nodal planes and the local orientation of the sill. While some sills exhibit significant nonplanarity, we observe that nodal planes hew closely to local structure even in the vicinity of undulations or kinks. To quantify the degree of alignment, we calculate a local tangent plane for each earthquake by fitting a plane to the 300 closest neighboring events and calculate the angle between this tangent plane and the most closely aligned nodal plane. Across the 10 structures, 87% (1250/1432) of events have nodal planes within 30° of the sill orientation (blue mechanisms in Figure 11). Within 9 of the 10 sills, including the two largest sills, > 86% of nodal planes align with the local sill orientation within 30°. We interpret this correspondence to mean that, for most of the seismicity in the PSC, slip occurs on the nodal plane aligned with the hosting sill structure.

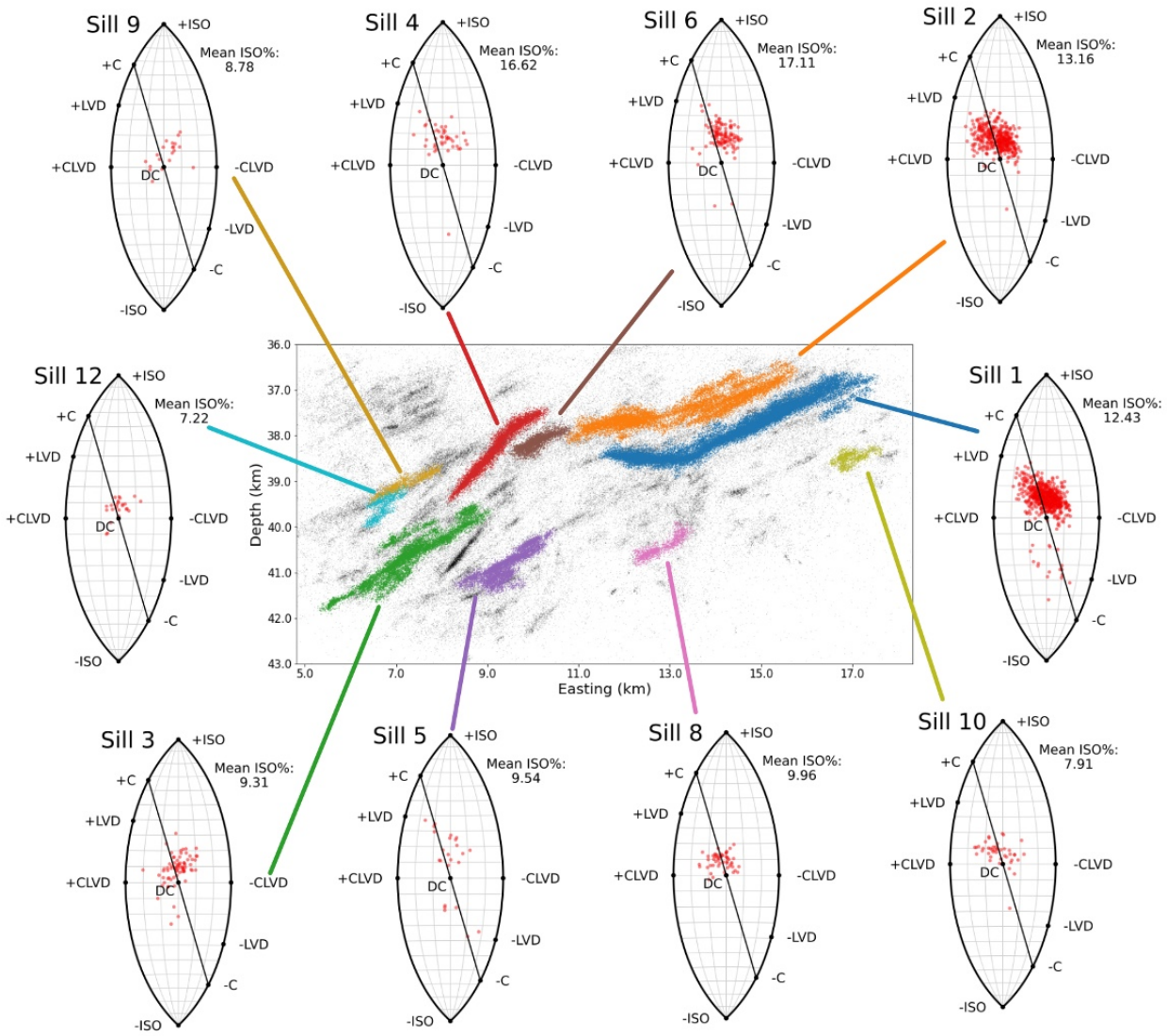

Figure 10: Summary of moment tensor solutions for each discrete structure in the PSC. Color-coding is to enhance visual clarity. Mean ISO% for each sill is reported next to the lune. Sills 7 and 11 have fewer than 10 high-quality solutions and are excluded from this plot.

The sense of slip for the majority of earthquakes is dominated by low-angle faulting, representative of an overriding block slipping seaward. This observation is consistent with most previous focal mechanism studies at southern Hawai'i, which have consistently reported approximately southward slumping on near-horizontal faults at depths from 10 to 30 km [Crosson and Endo 1981; Wolfe et al. 2003; 2004]. Our mechanisms are also consistent with composite fault-plane solutions previously derived for PSC events [Burgess and Roman 2021].

The azimuths of P axes across the PSC display a conspicuous radial pattern (Figure 12) consistent with previously reported mantle earthquake mechanisms in Hawai'i. Klein [2016] examined focal mechanisms below 21 km depth and found that P axis azimuths around the island of Hawai'i were oriented towards a point near the Mauna Loa summit. Klein [2016] inferred that this point represented the center of load stress exerted by the Mauna Loa and Mauna Kea volcanic piles and demonstrated that the radial pattern was consistent with a simple 2D cantilever model of flexural stress, implying a broken lithosphere under Hawai'i. Subsequent 3D stress modeling showed that this radial pattern could also be produced by flexural stress in an unbroken plate [Bellas and Zhong 2021].

The radial pattern we observe is centered on a point approximately 8 km to the east of Klein [2016]'s stress center (Figure 12). Although our center point and Klein's stress center were both determined by visual examination of P axis orientations, their locations agree well. We conclude that slip for the majority of earthquakes in the PSC is consistent with a flexural stress field produced by the Hawaiian island load.

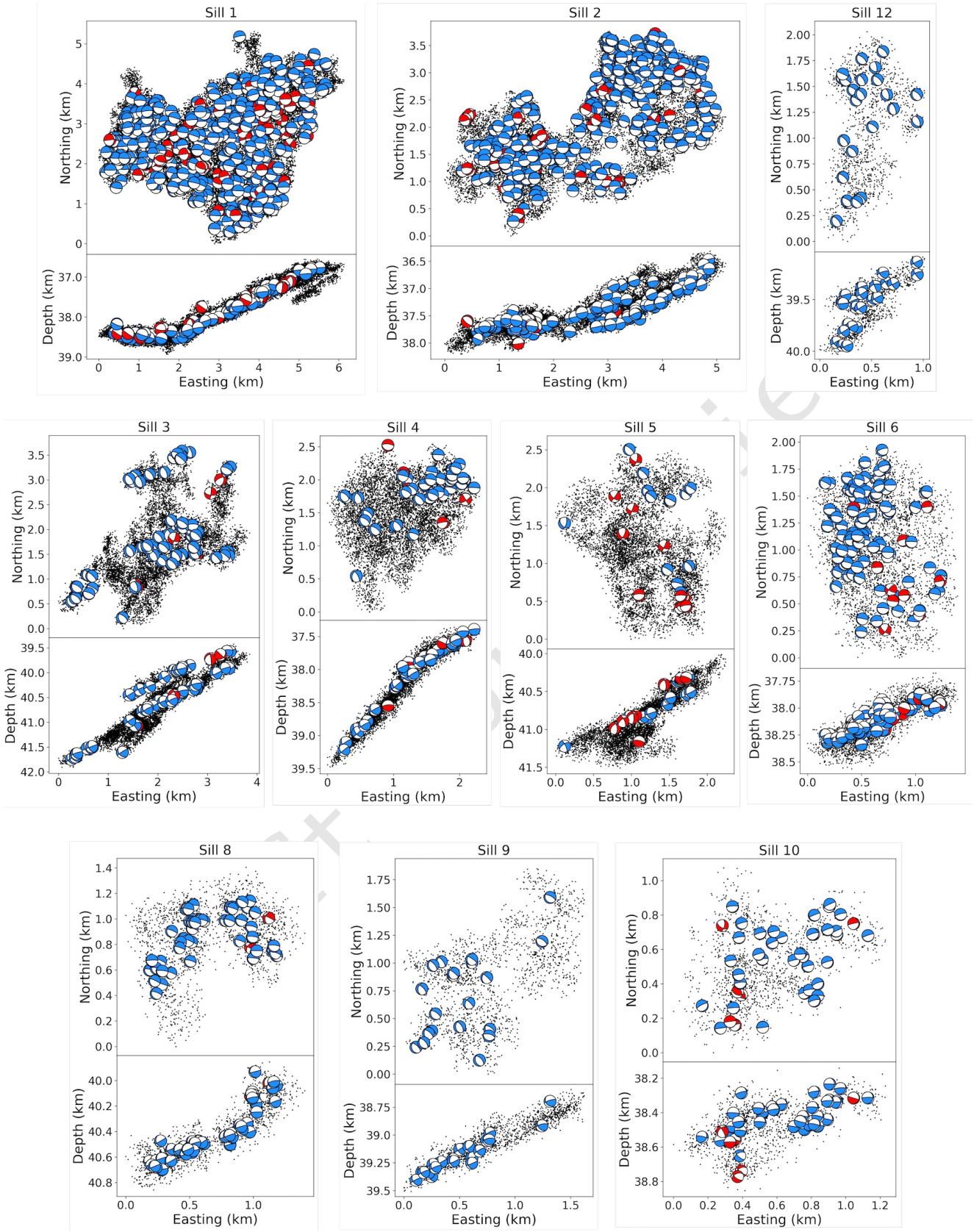

Figure 11: Double-couple components of high-quality moment tensors within 10 of the largest discrete structures in the PSC. Upper panels are map view and lower panels are east-west cross-sections. For the depth section plots, radiation patterns are projected onto the appropriate lower hemisphere for a north-facing viewing angle. Cross-sectional plots for sills 1 and 2 are limited to 150 mechanisms to preserve visibility. Moment tensors with a nodal plane within 30° of the local sill tangent plane are plotted in blue; other moment tensors are plotted in red.

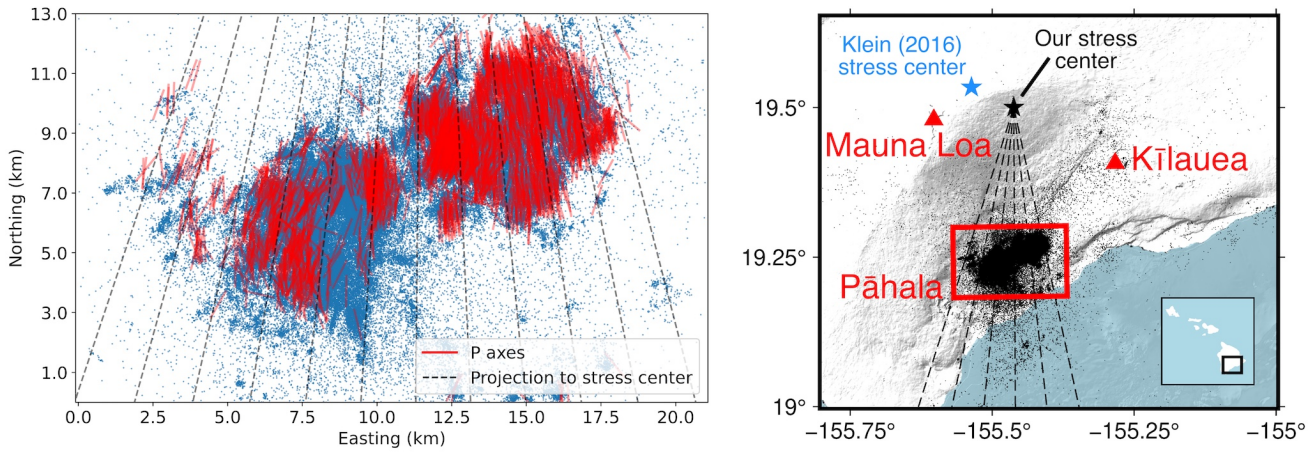

Figure 12: Map view of P axis azimuths plotted for all high-quality solutions. Left panel: P axes (red) display a radial pattern around a point near the Mauna Loa summit. Dashed lines illustrate the projection from this point to the PSC. PSC seismicity is plotted for visual reference. Right panel: map view of the PSC swarm, our visually determined stress center, and the visually determined stress center of Klein [2016].

4 Discussion

4.1 Seismogenic magma transport processes

Wilding et al. [2023] interpreted the highly productive, migrating earthquake swarms within the PSC as evidence of large-scale magma migration through sills. Migrating volcano-tectonic seismicity is frequently used to track magma dynamics in shallow crustal reservoirs and conduits [Klein et al. 1987; Ozawa et al. 2004; Ágústsdóttir et al. 2019], but inferred episodes of magmatic unrest in Hawaiian mantle are usually evidenced by long-period (LP) seismicity or tremor signals [Aki and Koyanagi 1981; Okubo and Wolfe 2008; Wech and Thelen 2015]. Our results provide a framework for understanding how apparent magma migration through the PSC is able to produce swarms of volcano-tectonic seismicity.

Previous authors have suggested that volcano-tectonic earthquakes beneath Pāhala are triggered by Coulomb stress transfer between inflated conduits and nearby pre-existing planes of weakness [Burgess and Roman 2021]. The correspondence we observe between nodal planes and local sill orientation in the PSC instead suggests that the slip occurs along the same planar structure responsible for transporting magma. The persistently observed contributions of positive isotropic source components to the shear-dominated faulting mechanisms also indicates that localized fluid-rock interactions might play a part in generating PSC seismicity. Similar tensile components have been documented in fluid-induced seismicity sequences near injection sites [Fischer and Guest 2011; Martínez-Garzón et al. 2017] and in volcanic environments [Dreger et al. 2000; Minson et al. 2007; Oliva et al. 2019; Hrubcová et al. 2021] and attributed to increased pore pressure along the slip surface. Seismicity in the PSC might be generated by a similar process if sufficient pre-existing differential stress acts upon fault planes. The presence of significant differential stress at the depth of the PSC is supported by previous large (M>4) earthquakes that have occurred beneath south Hawai'i below 25 km depth [USGS Hawaiian Volcano Observatory (HVO) 1956; Wolfe et al. 2004]. Stress modeling indicates that flexural stresses induced by the Mauna Loa and Mauna Kea volcanic loads are capable of reaching up to 100 MPa in the mantle [Bellas and Zhong 2021]. Because the radial pattern of P axes we observe is consistent with predictions from these stress models, we believe that the flexural stress field provides the necessary differential stress to prime structures in the PSC for fluid-induced seismicity.

We propose that magma migration in the PSC generates seismicity by relieving normal stress on the slip surface as it migrates along the slipping structures, enabling local patches to slip. This process is analogous to swarms generated by pore pressure diffusion in the crust [Hainzl 2004] and may be enabled at the depth of the PSC by flexurally derived differential stress. Similar compact, intensely seismogenic structures have not been identified elsewhere in the deep magma supply system of Hawai'i, possibly because vertically oriented slip planes are less favored to form in the radial-flexure stress field. Consequently, we may not expect to see similar patterns of seismogenesis in the vertical conduits beneath Kīlauea and Mauna Loa's summits, where magma transport may be dominated by buoyant flow.

4.2 Processes controlling magma transport beneath Hawai'i

Our model of seismogenesis in the PSC implies that sublateral magma transport in the Hawaiian mantle would concentrate along deep planes of weakness. Importantly, it also implies that deformation would concentrate along these features, and that this deformation would be promoted by magma transport. Interactions between magma supply processes and tectonic deformation have been extensively documented at basaltic shield volcanoes [Walter et al. 2005; Froger et al. 2015; Varugu and Amelung 2021]. These interactions can lead to positive feedback loops between magma processes and volcano deformation processes [Montgomery-Brown et al. 2015]. Such feedback is common between Kīlauea's East Rift Zone (ERZ) and flank décollement; magma intrusions into the ERZ can

stress the décollement, leading to earthquakes or slow slip, while décollement motion can unclamp the ERZ and promote magma intrusion [Montgomery-Brown et al. 2011]. If the stability of the magma-tectonic system is sufficiently disturbed by either process, runaway intrusion-décollement slip events can take place.

We suggest that a similar positive feedback loop could be sustaining the long-lasting productive seismic sequence in the PSC. In this model, a magma front propagating through one of the sills generates a highly productive sequence of earthquakes. These earthquakes result in spatially concentrated deformation and damage zones throughout the body of the sill. This concentrated damage may serve to increase permeability and promote future intrusive behavior, akin to fluid diffusion through fault damage zones in the crust following large earthquakes [Townend and Zoback 2000; Miller et al. 2004]. Together, these coupled processes may form a positive feedback loop leading to long-lived intrusions in the sill complex.

On long timescales, this feedback loop could sustain the growth and persistence of lateral magma transport structures in the PSC over many cycles of magma injection. On shorter timescales, positive feedback could result in sudden variations in magma flux rates through the sills and could serve as a viable mechanism to explain the rapid increases in earthquake rates measured in the PSC [Burgess and Roman 2021; Wilding et al. 2023]. Order-of-magnitude increases in PSC seismicity rates—likely signaling magma intrusion into the sills—were observed in 2015 and 2019 [Burgess and Roman 2021], with increased seismicity rates persisting through to the present day. The onset of the 2019 increase was contemporaneous with deep long-period seismicity 30 km below the Kīlauea summit and might have been spurred by pressure gradients propagating through Kīlauea's plumbing system [Wilding et al. 2023]. The increased seismic activity in 2015 was not preceded by seismic unrest elsewhere in Hawai'i's mantle magma system, although increased inflation began at Mauna Loa in 2014 [Thelen et al. 2017; Burgess and Roman 2021]. This inflationary phase might have increased flexural stresses on the PSC, generating favorable conditions for the initiation of a runaway deformation-intrusion feedback loop.

Unlike the 2015–present activity documented in Burgess and Roman [2021] and Wilding et al. [2023], the 2003-2007 magma surge to Mauna Loa and Kīlauea [Poland et al. 2012] did not coincide with a significant uptick in PSC seismicity. This observation suggests that the PSC was not active as a primary magma supply structure during this surge. Deep LP seismicity directly beneath the summit suggests that Mauna Loa was being supplied by a vertical conduit [Okubo and Wolfe 2008]. The existence of an alternative conduit connecting the PSC region to Mauna Loa was posited by Wright and Klein [2006]; Wilding et al. [2023] suggested that this Pāhala-Mauna Loa conduit may be acting as an active magma supply path to Mauna Loa during the ongoing surge. This sudden activation of the Pāhala-Mauna Loa conduit would suggest that distinct magma supply paths in the Hawaiian mantle can reactivate over relatively short timescales, in a manner similar to rift zone intrusions driven by cascading stress and pressure changes in Kīlauea's shallow magma system [Patrick et al. 2020]. Significant nonstationarity in the deep plumbing system may complicate interpretation of geochemical signatures in Hawaiian lavas. For instance, if different supply paths sample distinct regions of the underlying mantle plume, transient activation of alternative conduits may play a part in forming the temporally varying isotopic and trace element contents that have been observed in Hawaiian lavas [Rhodes et al. 1989; Pietruszka and Garcia 1999; Marske et al. 2008]. Our proposed mechanism would imply that structural factors within the deep plumbing system can contribute to dynamically modulating magma supply rates to the surface.

5 Conclusions

We compute high-quality moment tensors for 2,301 events in the Pahala Sill Complex to study magma transport processes in the Hawaiian mantle. For earthquakes hosted on large, subplanar sill structures, slip occurs in-plane with the structure. Source mechanisms include a component of tensile faulting, consistent with the presence of fluids in the slip plane. Earthquake P axes are consistent with the expectations for a flexural stress field from the Hawaiian island load, indicating that the differential stress at depths of 35-45 km may be sufficient for seismogenic magma transport within the PSC. We suggest that episodes of enhanced magma transport within the PSC may be enabled by a positive feedback loop between brittle deformation and magma intrusion, analogous to magmatic-tectonic interactions observed at Kilauea and other basaltic shield volcanoes. A runaway feedback loop may result in rapid increases in magma flux through the PSC and could be invoked to explain the ongoing mantle-driven magma surge to Kilauea and Mauna Loa. This model would imply that structural factors within the deep plumbing system can serve as an important control on magma supply rates to the surface.

Author Contributions

JDW and ZER conceptualized the project, implemented the methodology, analyzed the results, and contributed to writing and editing the manuscript.

Acknowledgements

The facilities of IRIS Data Services, and specifically the IRIS Data Management Center (DMC), were used for access to waveforms, related metadata, and/or derived products used in this study. IRIS Data Services are funded through the Seismological Facilities for the Advancement of Geoscience (SAGE) Award of the National Science Foundation under cooperative support agreement EAR-1851048.

Data Availability

Seismic data are publicly available from the IRIS DMC. The catalog and picks used in the moment tensor inversions are available upon request from the authors.

Copyright notice

References

Ágústsdóttir, T., T. Winder, J. Woods, R. S. White, T. Greenfield, and B. Brandsdóttir (2019). "Intense Seismicity During the 2014–2015 Bárðarbunga-Holuhraun Rifting Event, Iceland, Reveals the Nature of Dike-Induced Earthquakes and Caldera Collapse Mechanisms". *Journal of Geophysical Research: Solid Earth* 124(8), pages 8331–8357. DOI: 10.1029/2018JB016010.

Aki, K. and R. Koyanagi (1981). "Deep volcanic tremor and magma ascent mechanism under Kilauea, Hawaii". *Journal of Geophysical Research* 86(B8), page 7095. DOI: 10.1029/JB086iB08p07095.

Anderson, K. R. and M. P. Poland (2016). "Bayesian estimation of magma supply, storage, and eruption rates using a multiphysical volcano model: Kīlauea Volcano, 2000–2012". *Earth and Planetary Science Letters* 447, pages 161–171. DOI: 10.1016/j.epsl.2016.04.029.

Bellas, A. and S. J. Zhong (2021). "Seismic Strain Rate and Flexure at the Hawaiian Islands Constrain the Frictional Coefficient". *Geochemistry, Geophysics, Geosystems* 22(4). DOI: 10.1029/2020GC009547.

Brune, J. N. (1970). "Tectonic stress and the spectra of seismic shear waves from earthquakes". *Journal of Geophysical Research (1896-1977)* 75(26), pages 4997–5009. DOI: 10.1029/JB075i026p04997.

Burgess, M. K. and D. C. Roman (2021). "Ongoing (2015-) Magma Surge in the Upper Mantle Beneath the Island of Hawaii". *Geophysical Research Letters* 48(7), e2020GL091096. DOI: 10.1029/2020GL091096.

Cesca, S., J. Letort, H. N. T. Razafindrakoto, S. Heimann, E. Rivalta, M. P. Isken, M. Nikkhoo, L. Passarelli, G. M. Petersen, F. Cotton, and T. Dahm (2020). "Drainage of a deep magma reservoir near Mayotte inferred from seismicity and deformation". *Nature Geoscience* 13(1), pages 87–93. DOI: 10.1038/s41561-019-0505-5.

Crosson, R. S. and E. T. Endo (1981). "Focal mechanisms of earthquakes related to the 29 November 1975 Kalapana, Hawaii, earthquake: The effect of structure models". *Bulletin of the Seismological Society of America* 71(3), pages 713–729. DOI: 10.1785/BSSA0710030713.

Dreger, D. S., H. Tkalčić, and M. Johnston (2000). "Dilational Processes Accompanying Earthquakes in the Long Valley Caldera". *Science* 288(5463), pages 122–125. DOI: 10.1126/science.288.5463.122.

Dvorak, J. J. and D. Dzurisin (1993). "Variations in magma supply rate at Kilauea Volcano, Hawaii". *Journal of Geophysical Research: Solid Earth* 98(B12), pages 22255–22268. DOI: 10.1029/93JB02765.

Dzurisin, D. and M. P. Poland (2019). "Magma supply to Kīlauea Volcano, Hawai'i, from inception to now: Historical perspective, current state of knowledge, and future challenges". In: *Field Volcanology: A Tribute to the Distinguished Career of Don Swanson*. Geological Society of America. ISBN: 978-0-8137-2538-3. DOI: 10.1130/2018.2538(12).

Ebel, J. E. and K.-P. Bonjer (1990). "Moment tensor inversion of small earthquakes in southwestern Germany for the fault plane solution". *Geophysical Journal International* 101(1), pages 133–146. DOI: 10.1111/j.1365-246X.1990.tb00763.x.

Ester, M., H.-P. Kriegel, J. Sander, and X. Xu (1996). "A density-based algorithm for discovering clusters in large spatial databases with noise". In: *Proceedings of the Second International Conference on Knowledge Discovery and Data Mining*. KDD'96. Portland, Oregon: AAAI Press, pages 226–231.

Fischer, T. and A. Guest (2011). "Shear and tensile earthquakes caused by fluid injection". *Geophysical Research Letters* 38(5). DOI: 10.1029/2010GL045447.

Fitch, T. J., D. W. McCowan, and M. W. Shields (1980). "Estimation of the seismic moment tensor from teleseismic body wave data with applications to intraplate and mantle earthquakes". *Journal of Geophysical Research: Solid Earth* 85(B7), pages 3817–3828. DOI: 10.1029/JB085iB07p03817.

Froger, J.-L., V. Famin, V. Cayol, A. Augier, L. Michon, and J.-F. Lénat (2015). "Time-dependent displacements during and after the April 2007 eruption of Piton de la Fournaise, revealed by interferometric data". *Journal of Volcanology and Geothermal Research* 296, pages 55–68. DOI: 10.1016/j.jvolgeores.2015.02.014.

Greenfield, T., T. Winder, N. Rawlinson, J. Maclennan, R. S. White, T. Ágústsdóttir, C. A. Bacon, B. Brandsdóttir, E. P. S. Eibl, E. Glastonbury-Southern, E. Á. Gudnason, G. P. Hersir, and J. Horálek (2022). "Deep long period seismicity preceding and during the 2021 Fagradalsfjall eruption, Iceland". *Bulletin of Volcanology* 84(12), page 101. DOI: 10.1007/s00445-022-01603-2.

Hainzl, S. (2004). "Seismicity patterns of earthquake swarms due to fluid intrusion and stress triggering". *Geophysical Journal International* 159(3), pages 1090–1096. DOI: 10.1111/j.1365-246X.2004.02463.x.

Hieronymus, C. F. and D. Bercovici (1999). "Discrete alternating hotspot islands formed by interaction of magma transport and lithospheric flexure". *Nature* 397(6720), pages 604–607. DOI: 10.1038/17584.

Hrubcová, P., J. Doubravová, and V. Vavryčuk (2021). "Non-double-couple earthquakes in 2017 swarm in Reykjanes Peninsula, SW Iceland: Sensitive indicator of volcano-tectonic movements at slow-spreading rift". *Earth and Planetary Science Letters* 563, page 116875. DOI: 10.1016/j.epsl.2021.116875.

Huber, P. J. (1964). "Robust Estimation of a Location Parameter". *The Annals of Mathematical Statistics* 35(1), pages 73–101. DOI: 10.1214/aoms/1177703732.

Jaxybulatov, K., N. M. Shapiro, I. Koulakov, A. Mordret, M. Landès, and C. Sens-Schönfelder (2014). "A large magmatic sill complex beneath the Toba caldera". *Science* 346(6209), pages 617–619. DOI: 10.1126/science.1258582.

Jost, M. L. and R. B. Herrmann (1989). "A Student's Guide to and Review of Moment Tensors". *Seismological Research Letters* 60(2), pages 37–57. DOI: 10.1785/gssrl.60.2.37.

Klein, F. W. (1981). "A linear gradient crustal model for south Hawaii". *Bulletin of the Seismological Society of America* 71(5), pages 1503–1510. DOI: 10.1785/BSSA0710051503.

– (2016). "Lithospheric flexure under the Hawaiian volcanic load: Internal stresses and a broken plate revealed by earthquakes". *Journal of Geophysical Research: Solid Earth* 121(4), pages 2400–2428. DOI: 10.1002/2015JB012746.

Klein, F. W., R. Y. Koyanagi, J. S. Nakata, and W. R. Tanigawa (1987). "The seismicity of Kilauea's magma system". *USGS Professional Paper 1350: Volcanism in Hawaii*, pages 1019–1187. DOI: 10.3133/pp1350.

Kwiatek, G., P. Martínez-Garzón, and M. Bohnhoff (2016). "HybridMT: A MATLAB/Shell Environment Package for Seismic Moment Tensor Inversion and Refinement". *Seismological Research Letters* 87(4), pages 964–976. DOI: 10.1785/0220150251.

Lin, G., P. M. Shearer, F. Amelung, and P. G. Okubo (2015). "Seismic tomography of compressional wave attenuation structure for Kılauea Volcano, Hawai'i". *Journal of Geophysical Research: Solid Earth* 120(4), pages 2510–2524. DOI: 10.1002/2014JB011594.

Linzer, L. M. (2005). "A Relative Moment Tensor Inversion Technique Applied to Seismicity Induced by Mining". *Rock Mechanics and Rock Engineering* 38(2), pages 81–104. DOI: 10.1007/s00603-004-0041-4.

Liu, Q. and D. Wang (2016). "Stein Variational Gradient Descent: A General Purpose Bayesian Inference Algorithm". In: *Advances in Neural Information Processing Systems*. Volume 29. Curran Associates, Inc.

Marske, J. P., M. O. Garcia, A. J. Pietruszka, J. M. Rhodes, and M. D. Norman (2008). "Geochemical Variations during Kīlauea's Pu'u 'Ō'ō Eruption Reveal a Fine-scale Mixture of Mantle Heterogeneities within the Hawaiian Plume". *Journal of Petrology* 49(7), pages 1297–1318. DOI: 10.1093/petrology/egn025.

Martínez-Garzón, P., G. Kwiatek, M. Bohnhoff, and G. Dresen (2017). "Volumetric components in the earthquake source related to fluid injection and stress state". *Geophysical Research Letters* 44(2), pages 800–809. DOI: 10.1002/2016GL071963.

McGovern, P. J. (2007). "Flexural stresses beneath Hawaii: Implications for the October 15, 2006, earthquakes and magma ascent: FLEXURAL STRESSES BENEATH HAWAII". *Geophysical Research Letters* 34(23), n/a–n/a. DOI: 10.1029/2007GL031305.

Menke, W. and J. B. Russell (2020). "Non-Double-Couple Components of the Moment Tensor in a Transversely Isotropic Medium". *Bulletin of the Seismological Society of America* 110(3), pages 1125–1133. DOI: 10.1785/0120190319.

Miller, S. A., C. Collettini, L. Chiaraluce, M. Cocco, M. Barchi, and B. J. P. Kaus (2004). "Aftershocks driven by a high-pressure CO2 source at depth". *Nature* 427(6976), pages 724–727. DOI: 10.1038/nature02251.

Minson, S. E., D. S. Dreger, R. Bürgmann, H. Kanamori, and K. M. Larson (2007). "Seismically and geodetically determined nondouble-couple source mechanisms from the 2000 Miyakejima volcanic earthquake swarm". *Journal of Geophysical Research: Solid Earth* 112(B10). DOI: 10.1029/2006JB004847.

Montgomery-Brown, E. K., D. K. Sinnett, K. M. Larson, M. P. Poland, P. Segall, and A. Miklius (2011). "Spatiotemporal evolution of dike opening and décollement slip at Kīlauea Volcano, Hawai'i". *Journal of Geophysical Research: Solid Earth* 116(B3). DOI: 10.1029/2010JB007762.

Montgomery-Brown, E. K., M. P. Poland, and A. Miklius (2015). "Delicate Balance of Magmatic-Tectonic Interaction at Kīlauea Volcano, Hawai'i, Revealed from Slow Slip Events". In: *Hawaiian Volcanoes*. American Geophysical Union (AGU), pages 269–288. ISBN: 978-1-118-87207-9. DOI: 10.1002/9781118872079.ch13.

Okubo, P. G. and C. J. Wolfe (2008). "Swarms of similar long-period earthquakes in the mantle beneath Mauna Loa Volcano". *Journal of Volcanology and Geothermal Research* 178(4), pages 787–794. DOI: 10.1016/j.jvolgeores.2008.09.007.

Oliva, S. J., C. J. Ebinger, C. Wauthier, J. D. Muirhead, S. W. Roecker, E. Rivalta, and S. Heimann (2019). "Insights Into Fault-Magma Interactions in an Early-Stage Continental Rift From Source Mechanisms and Correlated Volcano-Tectonic Earthquakes". *Geophysical Research Letters* 46(4), pages 2065–2074. DOI: 10.1029/2018GL080866.

Ozawa, S., S. Miyazaki, T. Nishimura, M. Murakami, M. Kaidzu, T. Imakiire, and X. Ji (2004). "Creep, dike intrusion, and magma chamber deflation model for the 2000 Miyake eruption and the Izu islands earthquakes". *Journal of Geophysical Research: Solid Earth* 109(B2). DOI: 10.1029/2003JB002601.

Pacific Tsunami Warning Center (1965). *Pacific Tsunami Warning Seismic System*. DOI: 10.7914/SN/PT.

Patrick, M. R., B. F. Houghton, K. R. Anderson, M. P. Poland, E. Montgomery-Brown, I. Johanson, W. Thelen, and T. Elias (2020). "The cascading origin of the 2018 Kīlauea eruption and implications for future forecasting". *Nature Communications* 11(1), page 5646. DOI: 10.1038/s41467-020-19190-1.

Pietruszka, A. J. and M. O. Garcia (1999). "A Rapid Fluctuation in the Mantle Source and Melting History of Kilauea Volcano Inferred from the Geochemistry of its Historical Summit Lavas (1790–1982)". *Journal of Petrology* 40(8), pages 1321–1342. DOI: 10.1093/petroj/40.8.1321.

Poland, M. P., A. Miklius, A. Jeff Sutton, and C. R. Thornber (2012). "A mantle-driven surge in magma supply to Kīlauea Volcano during 2003–2007". *Nature Geoscience* 5(4), pages 295–300. DOI: 10.1038/ngeo1426.

Prieto, G. A., R. L. Parker, and F. L. Vernon III (2009). "A Fortran 90 library for multitaper spectrum analysis". *Computers & Geosciences* 35(8), pages 1701–1710. DOI: 10.1016/j.cageo.2008.06.007.

Prieto, G. A. (2022). "The Multitaper Spectrum Analysis Package in Python". *Seismological Research Letters* 93(3), pages 1922–1929. DOI: 10.1785/0220210332.

Pritchard, M. E., A. M. Rubin, and C. J. Wolfe (2007). "Do flexural stresses explain the mantle fault zone beneath Kilauea volcano?" *Geophysical Journal International* 168(1), pages 419–430. DOI: 10.1111/j.1365-246X.2006.03169.x.

Rhodes, J. M., K. P. Wenz, C. A. Neal, J. W. Sparks, and J. P. Lockwood (1989). "Geochemical evidence for invasion of Kilauea's plumbing system by Mauna Loa magma". *Nature* 337(6204), pages 257–260. DOI: 10.1038/337257a0.

Richards-Dinger, K. B. and P. M. Shearer (2000). "Earthquake locations in southern California obtained using source-specific station terms". *Journal of Geophysical Research: Solid Earth* 105(B5), pages 10939–10960. DOI: 10.1029/2000JB900014.

Rubin, A. M. (1995). "Propagation of Magma-Filled Cracks". *Annual Review of Earth and Planetary Sciences* 23(1). _eprint: https://doi.org/10.1146/annurev.ea.23.050195.001443, pages 287–336. DOI: 10.1146/annurev.ea.23.050195.001443.

Schumann, D. (2009). "Robust variable selection". PhD thesis. North Carolina State University.

Shapiro, N. M., D. V. Droznin, S. Y. Droznina, S. L. Senyukov, A. A. Gusev, and E. I. Gordeev (2017). "Deep and shallow long-period volcanic seismicity linked by fluid-pressure transfer". *Nature Geoscience* 10(6), pages 442–445. DOI: 10.1038/ngeo2952.

Shearer, P. M., R. E. Abercrombie, and D. T. Trugman (2022). "Improved Stress Drop Estimates for M 1.5 to 4 Earthquakes in Southern California From 1996 to 2019". *Journal of Geophysical Research: Solid Earth* 127(7), e2022JB024243. DOI: 10.1029/2022JB024243.

Shearer, P. M., G. A. Prieto, and E. Hauksson (2006). "Comprehensive analysis of earthquake source spectra in southern California". *Journal of Geophysical Research: Solid Earth* 111(B6). DOI: 10.1029/2005JB003979.

Smith, J. D., Z. E. Ross, K. Azizzadenesheli, and J. B. Muir (2022). "HypoSVI: Hypocentre inversion with Stein variational inference and physics informed neural networks". *Geophysical Journal International* 228(1), pages 698–710. DOI: 10.1093/gji/ggab309.

Swanson, D. A. (1972). "Magma Supply Rate at Kilauea Volcano, 1952-1971". *Science* 175(4018), pages 169–170. DOI: 10.1126/science.175.4018.169.

Swanson, D. A., T. R. Rose, A. E. Mucek, M. O. Garcia, R. S. Fiske, and L. G. Mastin (2014). "Cycles of explosive and effusive eruptions at Kīlauea Volcano, Hawai'i". *Geology* 42(7), pages 631–634. DOI: 10.1130/G35701.1.

Tape, W. and C. Tape (2012). "A geometric setting for moment tensors". *Geophysical Journal International* 190(1), pages 476–498. DOI: 10.1111/j.1365-246X.2012.05491.x.

Thelen, W., A. Miklius, and C. Neal (2017). "Volcanic Unrest at Mauna Loa, Earth's Largest Active Volcano". *Eos* 98. DOI: 10.1029/2017EO083937.

Townend, J. and M. D. Zoback (2000). "How faulting keeps the crust strong". *Geology* 28(5), pages 399–402. DOI: 10.1130/0091-7613(2000)28<399:HFKTCS>2.0.CO;2.

Trugman, D. T. (2020). "Stress-Drop and Source Scaling of the 2019 Ridgecrest, California, Earthquake Sequence". *Bulletin of the Seismological Society of America* 110(4), pages 1859–1871. DOI: 10.1785/0120200009.

Trugman, D. T. and P. M. Shearer (2017). "Application of an improved spectral decomposition method to examine earthquake source scaling in Southern California". *Journal of Geophysical Research: Solid Earth* 122(4), pages 2890–2910. DOI: 10.1002/2017JB013971.

– (2018). "Strong Correlation between Stress Drop and Peak Ground Acceleration for Recent M 1–4 Earthquakes in the San Francisco Bay Area". *Bulletin of the Seismological Society of America* 108(2), pages 929–945. DOI: 10.1785/0120170245.

USGS Hawaiian Volcano Observatory (HVO) (1956). *Hawaiian Volcano Observatory Network*. DOI: 10.7914/SN/HV.

Varugu, B. and F. Amelung (2021). "Southward growth of Mauna Loa's dike-like magma body driven by topographic stress". *Scientific Reports* 11(1), page 9816. DOI: 10.1038/s41598-021-89203-6.

Vavryčuk, V. (2011). "Tensile earthquakes: Theory, modeling, and inversion". *Journal of Geophysical Research: Solid Earth* 116(B12). DOI: 10.1029/2011JB008770.

– (2018). "Seismic Moment Tensors in Anisotropic Media: A Review". In: *Moment Tensor Solutions: A Useful Tool for Seismotectonics*. Edited by S. D'Amico. Springer Natural Hazards. Cham: Springer International Publishing, pages 29–54. ISBN: 978-3-319-77359-9. DOI: 10.1007/978-3-319-77359-9_2.

Walter, T. R., V. Acocella, M. Neri, and F. Amelung (2005). "Feedback processes between magmatic events and flank movement at Mount Etna (Italy) during the 2002–2003 eruption". *Journal of Geophysical Research: Solid Earth* 110(B10). DOI: 10.1029/2005JB003688.

Watanabe, T., T. Masuyama, K. Nagaoka, and T. Tahara (2002). "Analog experiments on magma-filled cracks: Competition between external stresses and internal pressure". *Earth, Planets and Space* 54(12), e1247–e1261. DOI: 10.1186/BF03352453.

Wech, A. G. and W. A. Thelen (2015). "Linking magma transport structures at Kīlauea volcano". *Geophysical Research Letters* 42(17), pages 7090–7097. DOI: 10.1002/2015GL064869.

Wilding, J. D., W. Zhu, Z. E. Ross, and J. M. Jackson (2023). "The magmatic web beneath Hawai'i". *Science* 379(6631), pages 462–468. DOI: 10.1126/science.ade5755.

Wolfe, C. J., P. G. Okubo, G. Ekström, M. Nettles, and P. M. Shearer (2004). "Characteristics of deep (≥13 km) Hawaiian earthquakes and Hawaiian earthquakes west of 155.55°W". *Geochemistry, Geophysics, Geosystems* 5(4). DOI: 10.1029/2003GC000618.

Wolfe, C. J., P. G. Okubo, and P. M. Shearer (2003). "Mantle Fault Zone Beneath Kilauea Volcano, Hawaii". *Science* 300(5618), pages 478–480. DOI: 10.1126/science.1082205.

Wright, T. L. and F. W. Klein (2006). "Deep magma transport at Kilauea volcano, Hawaii". *Lithos*. Mantle to Magma 87(1), pages 50–79. DOI: 10.1016/j.lithos.2005.05.004.

Wu, S.-M., H.-H. Huang, F.-C. Lin, J. Farrell, and B. Schmandt (2023). "Extreme seismic anisotropy indicates shallow accumulation of magmatic sills beneath Yellowstone caldera". *Earth and Planetary Science Letters* 616, page 118244. DOI: 10.1016/j.epsl.2023.118244.

Zhang, X. and A. Curtis (2020). "Variational full-waveform inversion". *Geophysical Journal International* 222(1), pages 406–411. DOI: 10.1093/gji/ggaa170.

Zhu, L. and D. V. Helmberger (1996). "Advancement in source estimation techniques using broadband regional seismograms". *Bulletin of the Seismological Society of America* 86(5), pages 1634–1641. DOI: 10.1785/BSSA0860051634.

Zhu, W. and G. C. Beroza (2019). "PhaseNet: a deep-neural-network-based seismic arrival-time picking method". *Geophysical Journal International* 216(1), pages 261–273. DOI: 10.1093/gji/ggy423.